Scripta Materialia 211 (2022) 114492

Contents lists available at ScienceDirect

Scripta Materialia

journal homepage: www.elsevier.com/locate/scriptamat

Oxidation resistance of cathodic arc evaporated $Cr_{0.74}Ta_{0.26}N$ coatings

Christina Kainz[a,*], Christian Saringer[a], Michael Burtscher[b], Michael Tkadletz[b], Andreas Stark[c], Norbert Schell[c], Markus Pohler[d], Christoph Czettl[d], Daniel Kiener[b], Nina Schalk[a]

[a] Christian Doppler Laboratory for Advanced Coated Cutting Tools at the Department of Materials Science, Montanuniversität Leoben, Franz-Josef-Straße 18, 8700 Leoben, Austria
[b] Department of Materials Science, Montanuniversität Leoben, Franz-Josef-Straße 18, 8700 Leoben, Austria
[c] Institute of Materials Physics, Helmholtz-Zentrum Hereon, Max-Planck-Straße 1, 21502 Geesthacht, Germany
[d] Ceratizit Austria GmbH, Metallwerk-Plansee-Straße 71, 6600 Reutte, Austria

ARTICLE INFO

Article history:
Received 22 December 2021
Revised 28 December 2021
Accepted 29 December 2021
Available online 7 January 2022

Keywords:
Protective coating
Oxidation
Synchrotron radiation
Transmission electron microscopy

ABSTRACT

Owing to their combination of high hardness and increased fracture toughness, CrTaN coatings have recently gained increasing interest as suitable candidates for metal cutting applications. However, up to now, the detailed mechanisms underlying the oxidation of this promising coating system are not thoroughly understood. Thus within this work, the evolution of microstructure and phase composition of a cathodic arc evaporated $Cr_{0.74}Ta_{0.26}N$ coating were illuminated in ambient atmosphere up to 1400 °C. *In situ* high-energy X-ray diffraction showed that powdered face-centered cubic (fcc) CrTaN displays an excellent oxidation resistance up to ~1050 °C, where the formation of tetragonal (t) $CrTaO_4$ and rhombohedral (r) Cr_2O_3 sets in. The compact CrTaN deposited on sapphire subjected to 1225 °C in ambient atmosphere exhibits intact fcc-CrTaN regions near the substrate, a porous intermediate layer of r-Cr_2O_3 and t-$CrTaO_4$ and a dense r-Cr_2O_3 oxide scale at the surface.

The ever-increasing demand in the metal cutting industry for higher productivity and longer tool lifetime asks for sophisticated protective hard coatings. Whereas the positive effect on hardness and thermal stability upon Al or Si addition to CrN is extensively reviewed in literature, ternary CrTaN coatings have only recently gained interest [1–5]. While CrN exhibits the face-centered cubic (fcc) structure, TaN occurs in various modifications. Here, the hexagonal (h) π-TaN and the h-θ-TaN are energetically favored over metastable fcc-TaN [6,7]. CrTaN coatings grown by physical vapor deposition (PVD) are, however, reported to crystallize in an fcc-$Cr_xTa_{1-x}N$ solid solution, which is attributed to the non-equilibrium conditions of the process. Both, magnetron sputtering as well as cathodic arc evaporation (CAE) can be used to synthesize CrTaN coatings with a hardness of up to 27 GPa [8,9]. In addition to good tribological properties [9], CrTaN coatings have furthermore shown to exhibit a promising fracture toughness and beneficial performance during thermal cycling [10,11].

Since hard coatings are subjected to high thermal load with simultaneous oxidative attack during application, their oxidation resistance is of major importance. Chen et al. have investigated the effect of an annealing treatment in air on sputter-deposited CrTaN coatings. The authors observed a thin oxide scale containing rhombohedral (r) Cr_2O_3 and orthorhombic (o) Ta_2O_5 when oxidizing the coatings at 500 °C for 4 h. Increasing the temperature to 600 °C for the same duration resulted in a significantly more pronounced oxidation [8]. As a result, the mechanical properties of the coatings deteriorated. In addition to r-Cr_2O_3 and o-Ta_2O_5, the formation of tetragonal (t) $CrTaO_4$ as an oxidation product of CrTaN based coatings is reported [12]. However, up to now, the detailed oxidation sequence of CrTaN as a function of the temperature has not been investigated. Thus, the present work aims to elucidate the oxidation mechanism of CAE CrTaN coatings employing a combinatorial approach of synchrotron X-ray diffraction (XRD), differential scanning calorimetry (DSC), thermo-gravimetric analysis (TGA), scanning and transmission electron microscopy as well as energy-dispersive X-ray spectroscopy (EDX).

The investigated CrTaN coating was deposited in an industrial scale Oerlikon Balzers INNOVA arc evaporation system at a bias voltage of −60 V. Three powder metallurgically produced compound targets with a composition of 75 at% Cr and 25 at% Ta were used to grow the coating. For further information on the target arrangement and deposition conditions, the reader is referred

* Corresponding author.
E-mail address: christina.kainz@unileoben.ac.at (C. Kainz).

https://doi.org/10.1016/j.scriptamat.2021.114492

to ref. [10]. The used substrates, being mild steel foil and single crystalline sapphire with (001) orientation, were subjected to two- and three-fold rotation within the carousel, respectively. To obtain the coating powder, the mild steel foil was dissolved after deposition using nitric acid. The elemental composition of the coating was quantified by glow discharge optical emission spectroscopy (GDOES) using a GD-Profiler 2 by Horiba. A first assessment of the microstructure was realized by lab-scale XRD. A Bruker AXS D8 Advance diffractometer with CuK_α radiation, operated in Bragg-Brentano geometry, was used for this purpose. The residual stress of the coating on sapphire was determined applying the $\sin^2\psi$ method in side-inclination on the 111 peak with $\sin^2\psi$ values between 0 and 0.55. The respective X-ray elastic constants were calculated using the Hill grain interaction model, with calculated elastic constants from fcc-CrN [13] and fcc-TaN [14]. A cross-sectional micrograph of the as-deposited coating was obtained using a scanning electron (SE) microscope of type Auriga from Zeiss.

High energy XRD experiments were carried out at the high energy materials science beamline P07 operated by the Helmholtz-Zentrum Hereon at the PETRA III storage ring at DESY in Hamburg [15]. Powdered CrTaN was placed in a Pt crucible, which was inductively heated in ambient atmosphere between 100 and 1400 °C at a heating rate of 20 °C/min. The wavelength of the X-ray beam was 0.11965 Å and Debye-Scherrer rings were collected in transmission geometry on a digital Perkin Elmer XRD 1621 2D X-ray detector every ~5 °C. Azimuthal integration of the Debye-Scherrer rings in order to obtain one-dimensional diffractograms was conducted with the software DAWN2 [16]. Subsequently, quantitative phase analysis by sequential Rietveld refinement for each diffractogram was realized using the software TOPAS 6 by Bruker [17,18]. The crystallographic information files (cif) used for the refinement of the individual phases were taken from the Crystallography Open Database [19]. DSC experiments on CrTaN powders were performed in Al_2O_3 crucibles on a Setaram Setsys EVO 2400 calorimeter in synthetic air. The same heating rate and maximum temperature as used in the synchrotron radiation experiment were applied.

The phase evolution of the compact coating on sapphire during oxidation was investigated by *in-situ* high temperature XRD. The above-mentioned diffractometer, equipped with a heating chamber type HTK 1200 N by Anton Paar, was used to realize the experiments. The diffractograms were recorded between RT and 1200 °C in steps of 25 °C at a heating rate of ~2.5 °C/min. In addition, a virgin CrTaN coating deposited on sapphire was oxidized in the aforementioned calorimeter up to 1225 °C with a heating rate of 20 °C/min. The maximum temperature was held for 15 min. Using an SE microscope type Gemini 450 from Zeiss, the cross-sectional microstructure of the partly oxidized coating was studied. The microscope is equipped with an Ultim Extreme detector by Oxford Instruments for EDX mapping. A lamella for transmission electron microscopy (TEM) investigations was prepared applying the lift-out technique on a dual-beam workstation by FEI. High-resolution TEM (HRTEM) was performed using a microscope type JEOL 2200FS, which was operated at an acceleration voltage of 200 kV. The microscope is equipped with a field emission gun and a TVIPS TemCam of type XF416 for high-resolution imaging. Further image processing and data analysis were performed using the free software package GMS 3.4.3 from Gatan.

The elemental composition of the coating was determined to 37 at% Cr, 13 at% Ta and 50 at% N by GDOES. Thus, the Cr/(Cr+Ta) ratio in the coating (0.74) is within the accuracy of the chosen quantification method comparable to that in the target (0.75). A cross-sectional micrograph of the CrTaN coating on sapphire is shown in Fig. 1a. The grains appear elongated and do not extend throughout the whole coating thickness. As typical for competitive growth, the grain size increases with increasing coating thickness [20]. Furthermore, the presence of a layered structure is evident, which can be attributed to the three-fold rotation during deposition [21]. Fig. 1b shows the X-ray diffractograms of CrTaN on sapphire and the powdered coating recorded at the lab-scale XRD and storage ring, respectively. Since the lab-scale and synchrotron measurements were conducted at different photon energies, the d-spacing rather than the 2θ angle is given within this work to provide better comparability. In both cases, all reflections are located between the standard peak positions of fcc-CrN [22] and fcc-TaN [23], confirming the presence of an fcc-$Cr_xTa_{1-x}N$ solid solution. The diffraction peaks are shifted to larger d-spacings in case of the coating on sapphire in comparison to the powder. This observation can be attributed to the compressive stress of the coating on sapphire, which amounts to -3.3 ± 0.3 GPa. While the 200 reflection is most pronounced in case of the powdered coating, the 311 reflection is dominant in the CrTaN coating on sapphire, indicating a preferred <311> orientation.

The 2D Debye Scherrer rings recorded during the synchrotron radiation experiment were transformed into 1D diffractograms by azimuthal integration. Fig. 2a shows the resulting phase plot of the CrTaN powder between 100 and 1400 °C. Three different temperature-dependent zones can be differentiated, which are marked by the formation or disappearance of crystallographic phases. Up to ~1050 °C (zone 1), no additional crystalline phases to fcc-$Cr_xTa_{1-x}N$ can be observed. Thus, the oxidation resistance of CrTaN is significantly higher than the one reported for fcc-CrN (~700 °C) and fcc-TaN (~700 °C) [24–26]. It is evident that the diffraction peaks shift to higher d-spacings as the temperature increases, which can be attributed to the thermal expansion of the lattice. At ~1050 °C (zone 2) a second phase emerges, which is ascribed to t-$CrTaO_4$ [27]. This is reported to form at temperatures >950 °C and was found as an oxidation product of compact CrTaN coatings [12,28]. Slightly delayed at ~1100 °C, the formation of r-Cr_2O_3 [29] starts, which is frequently observed as an oxidation product of CrN based coatings [12,24,30]. At ~1275 °C, the nitride has completely transformed into t-$CrTaO_4$ and r-Cr_2O_3 (zone 3). Upon further increasing the temperature, the phase plot does not indicate any additional reactions. To study the oxidation onset more precisely and to quantify the phase fraction of the nitride and oxides, sequential Rietveld refinement was applied (Fig. 2b). Prior to 1050 °C, including the oxides in the refinement does not result in a significant contribution by them. Thus, at lower temperatures, the powder is assumed to consist only of fcc-$Cr_xTa_{1-x}N$. The onset of t-$CrTaO_4$ formation according to the refinement at 1050 °C is in good agreement with the impression from the phase plot. The transformation of the nitride into the oxides occurs in a narrow temperature range of ~225 °C, resulting in complete oxidation of the powder at ~1275 °C. According to the phase quantification, the ratio between t-$CrTaO_4$ and r–Cr_2O_3 does not change significantly after the nitride has completely transformed into oxides.

The heat flow and mass change related to the oxidation of the powder is shown in Fig. 2c. A pronounced exothermic peak is evident between ~1050 and 1300 °C, which is attributed to the oxidation of fcc-$Cr_xTa_{1-x}N$ to t-$CrTaO_4$ and r-Cr_2O_3. From the kink in the heat flow curve at ~1150 °C a two-step reaction may be suggested. This hypothesis is substantiated by the slightly delayed onset of r-Cr_2O_3 formation observed in the synchrotron experiments. The overall mass increment upon oxidation amounts to ~13.5%, which meets the stoichiometric prediction at the given Cr/(Cr+Ta) ratio. Finally, it should be mentioned that the peak temperatures from the respective decomposition and oxidation reaction as determined by the DSC-TGA experiments are well in line with the findings from the synchrotron radiation experiment.

To assess the oxidation resistance of the compact coating, CrTaN on sapphire was heated in ambient atmosphere and the phase evolution was studied by *in-situ* high temperature XRD. Since the used heating chamber allows a maximum temperature of 1200 °C,

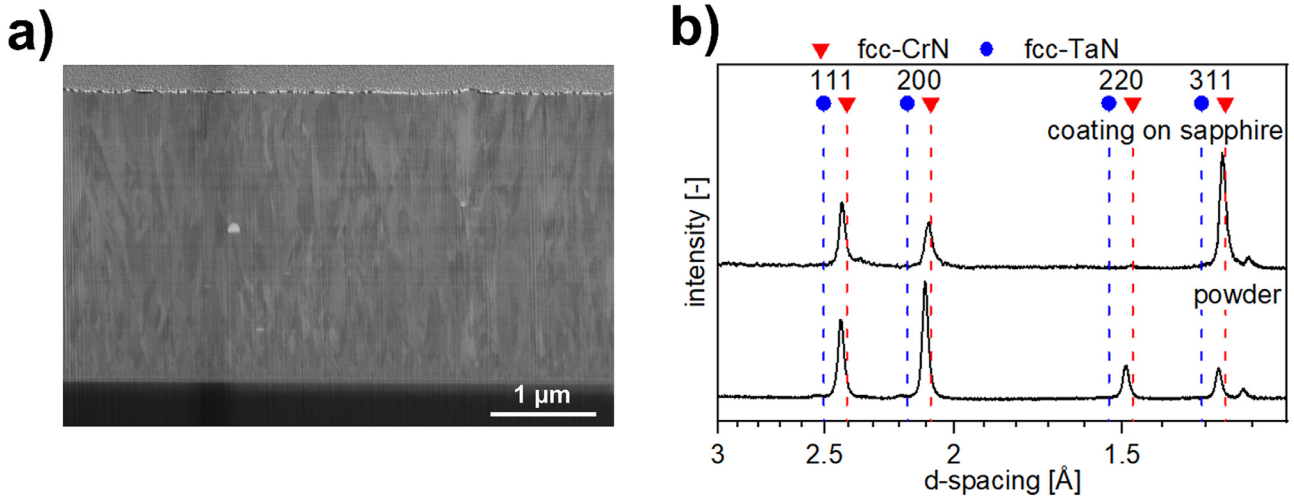

Fig. 1. (a) Cross-sectional secondary electron micrograph and (b) X-ray diffractogram of CrTaN on sapphire in as-deposited state. The X-ray diffractogram of powdered CrTaN is shown as well.

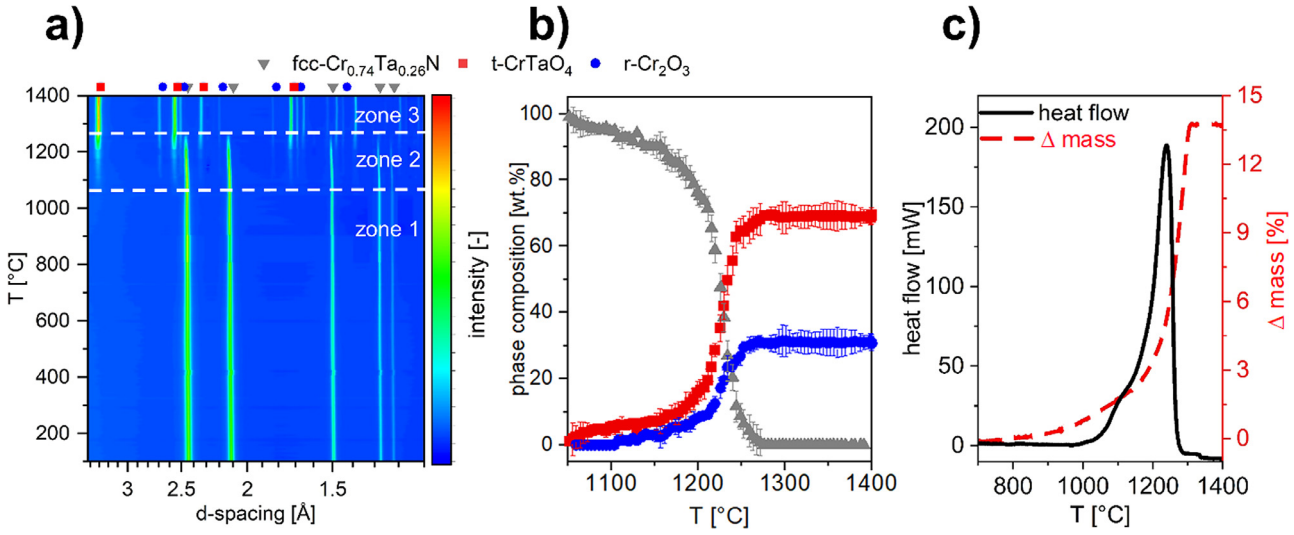

Fig. 2. a) Phase evolution of powdered CrTaN in air between 100 and 1400 °C as obtained from the synchrotron radiation experiment. The standard peak positions of fcc-$Cr_{0.74}Ta_{0.26}N$, t-$CrTaO_4$ and r-Cr_2O_3 at RT are given as well. b) Quantitative phase composition of the CrTaN powder in the temperature range from 1050–1400 °C as determined by quantitative Rietveld refinement. c) The heat flow and mass change data determined from the DSC/TGA experiment.

the recorded diffractograms in Fig. 3a are depicted for a temperature range between RT and 1200 °C. As for the powdered CrTaN, r-Cr_2O_3 and t-$CrTaO_4$ evolve upon oxidation of the compact coating. However, a lower oxidation onset was observed in case of the compact coating on sapphire compared to the powder. This counterintuitive observation can be attributed to the significantly lower heating rate of the lab-scale experiment (~2.5 °C/min) than in the synchrotron study (20 °C/min).

An additional sample was heated within the DSC to 1225 °C at 20 °C/min, which allowed the investigation of a partly oxidized coating. The SE micrograph in Fig. 3b shows that the partly oxidized coating consists of three zones. In zone 1, coarse equiaxed grains, which are significantly larger compared to the ones observed in the as-deposited state (Fig. 1a), are visible. These coarser grains appear to be non-oxidized, since still a high fraction of N and no O was detected within them. In contrast, the EDX mapping in Fig. 3c shows that the grain boundaries provide significant diffusion pathways for O, allowing oxidational processes to proceed into deeper zones of the coating along its grain boundaries. From the EDX maps of O and N it is evident that the coating is entirely oxidized within zone 2, where also some porous domains within the material are present. Both, regions rich in Ta, which can be attributed to t-$CrTaO_4$, and regions rich in Cr, corresponding to r-Cr_2O_3, can be identified. Within the outermost layer, no Ta was found, indicating that zone 3 consists entirely of r-Cr_2O_3. It appears that this region is significantly denser than the underlying intermediate zone 2. This observation is in agreement with literature, since r-Cr_2O_3 is reported to form a dense oxide scale [8,31]. As Chen et al. have shown, CrTaN coatings exhibit a high hardness not only in as-deposited state, but also after partial oxidation as a result of thermal cycling [11].

TEM investigations allowed to obtain a detailed insight into the nanoscale structure of the partly oxidized coating within the respective zones. A scanning TEM (STEM) overview micrograph, as well as high resolution images of the intact CrTaN regions, the intermediate porous layer and the dense surface oxide scale, are shown in Fig. 4. In addition, fast Fourier transformation (FFT) images recorded from selected areas are displayed in Fig. 4. From the STEM image in Fig. 4a it is evident that the largest grains are present within the intact CrTaN layer, whereas the intermediate layer accommodates the smallest grains. The d-spacing determined by FFT and inverse FFT (IFFT) within a grain in the intact CrTaN

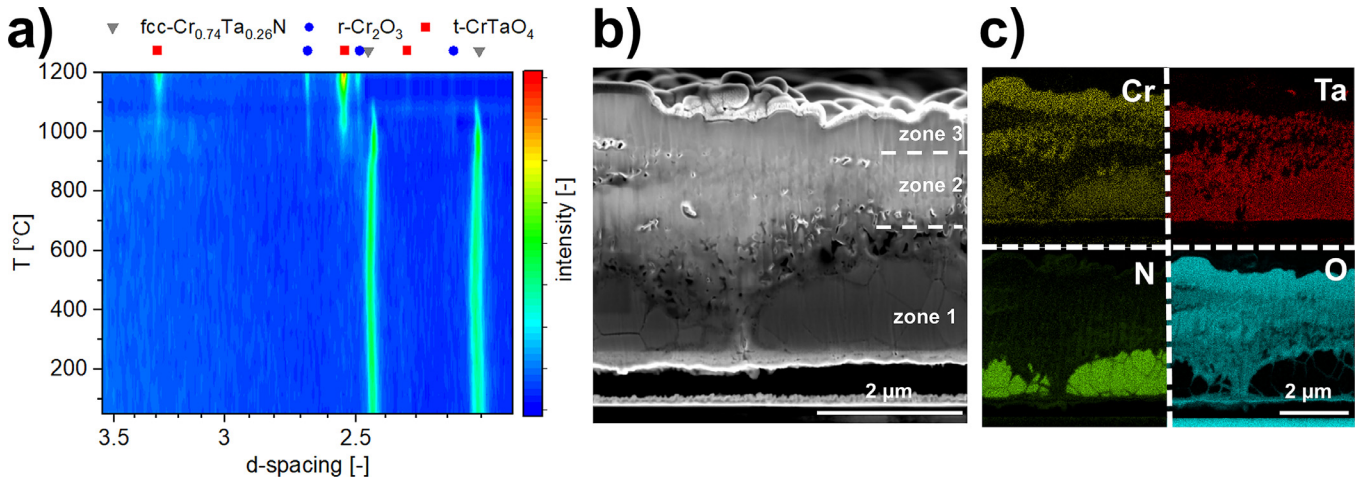

Fig. 3. Oxidation resistance of CrTaN on sapphire: a) The phase evolution of CrTaN on sapphire in air between RT and 1200 °C as determined by XRD. b) Secondary electron micrograph and c) Cr, Ta, N and O elemental maps recorded on a partly oxidized CrTaN coating.

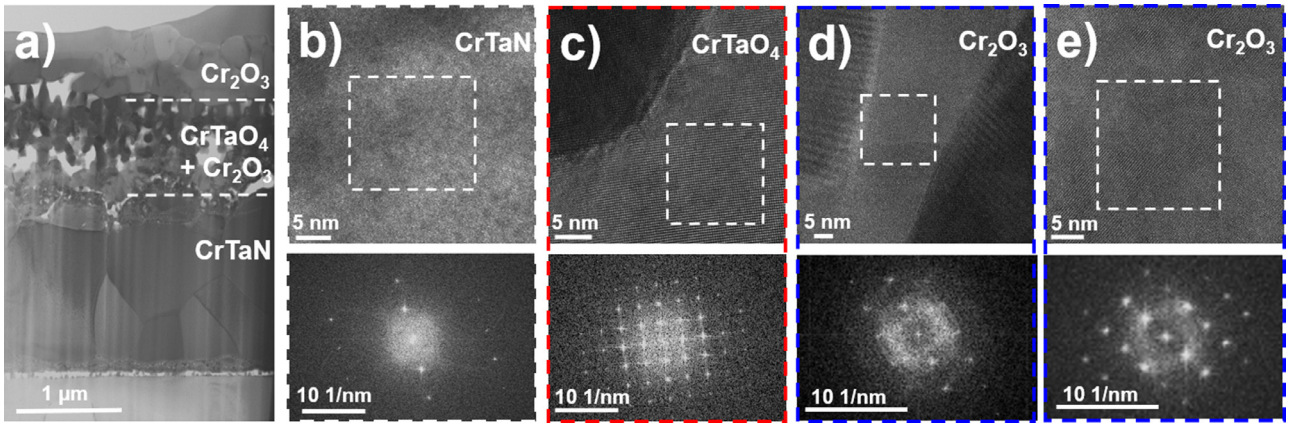

Fig. 4. a) STEM image of the partly oxidized CrTaN coating on sapphire. High resolution micrographs (top) and corresponding FFT images (bottom) of b) the intact CrTaN region, the porous intermediate layer accommodating c) $CrTaO_4$ and d) Cr_2O_3 and e) the dense surface-near Cr_2O_3 layer.

layer (Fig. 4b) amounted to 2.4 Å, which can be attributed to the interplanar spacing of fcc-$Cr_xTa_{1-x}N$ (111 planes) [32,33]. Within the intermediate layer in Fig. 4c, interplanar spacings corresponding to the (110) planes of t-$CrTaO_4$ (3.3 Å) were identified [34]. In addition, interplanar spacings of 3.6 Å were detected within the intermediate layer in Fig. 4d, which can be ascribed to the (012) planes of r-Cr_2O_3 [35]. This observation confirms that the intermediate layer includes both, r-Cr_2O_3 and t-$CrTaO_4$ grains. In case of the dense surface oxide scale (Fig. 4e), only interplanar spacings reported for r-Cr_2O_3, e.g. 3.7 Å, could be determined.

Within this study, crystallographic, calorimetric and microscopic characterization techniques were complementarily applied to investigate the oxidation resistance of a $Cr_{0.74}Ta_{0.26}N$ coating deposited by CAE. High-energy XRD at a synchrotron radiation facility showed that powdered CrTaN exhibits a high resistance against oxidative attack, since the first oxidation products are only observed at ~1050 °C. Upon increasing the temperature to higher values, the fcc-$Cr_xTa_{1-x}N$ solid solution transforms into t-$CrTaO_4$ and r-Cr_2O_3. The same oxidation products are observed, when a solid CrTaN coating on sapphire is subjected to a heat treatment in air. From a partly oxidized coating heated to 1225 °C, the presence of three zones was identified: intact coarse-grained fcc-CrTaN regions at the interface to the substrate, a porous intermediate layer of r-Cr_2O_3 and t-$CrTaO_4$ and a dense r-Cr_2O_3 oxide scale at the surface. The obtained data allow detailed insights into the oxidation of CrTaN and confirm the suitability of (Cr,Ta)N based coatings for application in demanding conditions such as metal cutting or glass molding.

The financial support by the Austrian Federal Ministry for Digital and Economic Affairs and the National Foundation for Research, Technology and Development is gratefully acknowledged. The authors furthermore acknowledge funding by the European Research Council (Grant number: 771146). We thank Dr. Jarosław Wosik (Materials Center Leoben) and Dr. Julian Wagner (Materials Center Leoben) for SEM/FIB/EDX work. The authors acknowledge DESY (Hamburg, Germany), a member of the Helmholtz Association HGF, for the provision of experimental facilities.

Declaration of Competing Interest

The authors declare that they have no known competing financial interests or personal relationships that could have appeared to influence the work reported in this paper.

References

[1] H. Willmann, P.H. Mayrhofer, P.O.Å. Persson, A.E. Reiter, L. Hultman, C. Mitterer, Scripta Mater. 54 (2006) 1847–1851.
[2] H. Willmann, P.H. Mayrhofer, L. Hultman, C. Mitterer, Int. Heat Treat. Surf. Eng. 1 (2007) 75–79.
[3] P.H. Mayrhofer, H. Willmann, A.E. Reiter, Surf. Coat. Technol. 202 (2008) 4935–4938.
[4] H.Y. Lee, W.S. Jung, J.G. Han, S.M. Seo, J.H. Kim, Y.H. Bae, Surf. Coat. Technol. 200 (2005) 1026–1030.

[5] T. Polcar, A. Cavaleiro, Mater. Chem. Phys. 129 (2011) 195–201.
[6] M. Grumski, P.P. Dholabhai, J.B. Adams, Acta Mater. 61 (2013) 3799–3807.
[7] N. Koutná, D. Holec, O. Svoboda, F.F. Klimashin, P.H. Mayrhofer, J. Phys. D: Appl. Phys. 49 (2016) 375303.
[8] Y.-.I. Chen, Y.-.T. Lin, L.-.C. Chang, J.-.W. Lee, Surf. Coat. Technol. 206 (2011) 1640–1647.
[9] N. Schalk, M. Pohler, S. Hirn, V.T. Terziyska, P. Polcik, S. Kolozsvári, C. Mitterer, C. Czettl, Int. J. Refract. Met. Hard Mater. 71 (2018) 211–216.
[10] C. Kainz, M. Pohler, G.C. Gruber, M. Tkadletz, A.S. Ebner, C. Czettl, N. Schalk, Surf. Coat. Technol. 417 (2021) 127212.
[11] Y.-.I. Chen, K.-.Y. Lin, H.-.H. Wang, K.-.C. Lin, Surf. Coat. Technol. 259 (2014) 159–166.
[12] M. Cekada, P. Panjan, B. Navinsek, F. Cvelbar, Vacuum 52 (1999) 461–467.
[13] J. Almer, U. Lienert, R.L. Peng, C. Schlauer, M. Odén, J. Appl. Phys. 94 (2003) 697–702.
[14] J. Chang, G.-.P. Zhao, X.-.L. Zhou, K. Liu, L.-.Y. Lu, J. Appl. Phys. 112 (2012) 083519.
[15] N. Schell, A. King, F. Beckmann, T. Fischer, M. Müller, A. Schreyer, MSF 772 (2013) 57–61.
[16] M. Basham, J. Filik, M.T. Wharmby, P.C.Y. Chang, B. El Kassaby, M. Gerring, J. Aishima, K. Levik, B.C.A. Pulford, I. Sikharulidze, D. Sneddon, M. Webber, S.S. Dhesi, F. Maccherozzi, O. Svensson, S. Brockhauser, G. Náray, A.W. Ashton, J. Synchrotron Radiat. 22 (2015) 853–858.
[17] R.A. Young, The Rietveld Method, Oxford University Press, Oxford, New York, 1993.
[18] C. Saringer, M. Tkadletz, A. Stark, N. Schell, C. Czettl, N. Schalk, Surf. Coat. Technol. 374 (2019) 617–624.
[19] , Crystallography Open Database (2019) http://www.crystallography.net.
[20] P.B. Barna, M. Adamik, J. Lábár, L. Kövér, J. Tóth, A. Dévényi, R. Manaila, Surf. Coat. Technol. 125 (2000) 147–150.
[21] M. Panjan, Surf. Coat. Technol. 235 (2013) 32–44.
[22] M. Widenmeyer, E. Meissner, A. Senyshyn, R. Niewa, Z. Anorg. Allg. Chem. 640 (2014) 2801.
[23] T. Mashimo, S. Tashiro, T. Toya, M. Nishida, H. Yamazaki, S. Yamaya, K. Oh-ishi, Y. Syono, J. Mater. Sci. 28 (1993) 3439–3443.
[24] Y.C. Chim, X.Z. Ding, X.T. Zeng, S. Zhang, Thin Solid Films 517 (2009) 4845–4849.
[25] H.O. Pierson, Handbook of Refractory Carbides and Nitrides: Properties, Characteristics, Processing, and Applications, Noyes Publications, New York, 1996.
[26] K. Hamaguchi, T. Tsuchiyama, J. Matsushita, Mater. Sci. Forum 761 (2013) 125–129.
[27] W. Wong-Ng, H.F. McMurdie, B. Paretzkin, C.R. Hubbard, A. Dragoo, Powder Diffraction,, 3rd ed., 1988.
[28] C. Keller, Z. Anorg. Allg. Chem. 318 (1962) 89–106.
[29] H.E. Swanson, H.F. McMurdie, M.C. Morris, E.H. Evans, Standard X-ray Diffraction Powder Patterns, 25th ed., 1955.
[30] J.-.J. Moon, D.-.J. Kim, D.-.B. Lee, Met. Mater. Int. 8 (2002) 211–214.
[31] Darius Tytko, Pyuck-Pa Choi, Dierk Raabe, Nano Converg 4 (2017) 1–5.
[32] International centre for diffraction data, PDF-2 Release, 01-083-5612.
[33] International centre for diffraction data, PDF-2 Release, 00-049-1283.
[34] International centre for diffraction data, PDF-2 Release, 00-039-1428.
[35] International centre for diffraction data, PDF-2 Release, 00-006-0504